Liquid lithium divertor characteristics and plasma–material interactions in NSTX high-performance plasmas

2013 Nucl. Fusion 53 083032

(http://iopscience.iop.org/0029-5515/53/8/083032)

Nucl. Fusion **53** (2013) 083032 (9pp) doi:10.1088/0029-5515/53/8/083032

Liquid lithium divertor characteristics and plasma–material interactions in NSTX high-performance plasmas

M.A. Jaworski[1], T. Abrams[1], J.P. Allain[2], M.G. Bell[1], R.E. Bell[1], A. Diallo[1], T.K. Gray[3], S.P. Gerhardt[1], R. Kaita[1], H.W. Kugel[1], B.P. LeBlanc[1], R. Maingi[3], A.G. McLean[4], J. Menard[1], R. Nygren[5], M. Ono[1], M. Podesta[1], A.L. Roquemore[1], S.A. Sabbagh[6], F. Scotti[1], C.H. Skinner[1], V.A. Soukhanovskii[4], D.P. Stotler[1] and the NSTX Team

[1] Princeton Plasma Physics Laboratory, Princeton, NJ 08543, USA
[2] School of Nuclear Engineering, Purdue University, West Lafayette, IN 47907, USA
[3] Oak Ridge National Laboratory, Oak Ridge, TN 37831, USA
[4] Lawrence Livermore National Laboratory, Livermore, CA 94551, USA
[5] Sandia National Laboratory, Albuquerque, NM 87185, USA
[6] Department of Applied Physics and Applied Mathematics, Columbia University, New York, NY 10027, USA

E-mail: mjaworsk@pppl.gov

Received 31 December 2012, accepted for publication 25 June 2013
Published 30 July 2013
Online at stacks.iop.org/NF/53/083032

Abstract
Liquid metal plasma-facing components (PFCs) have been proposed as a means of solving several problems facing the creation of economically viable fusion power reactors. To date, few demonstrations exist of this approach in a diverted tokamak and we here provide an overview of such work on the National Spherical Torus Experiment (NSTX). The Liquid Lithium Divertor (LLD) was installed and operated for the 2010 run campaign using evaporated coatings as the filling method. The LLD consisted of a copper-backed structure with a porous molybdenum front face. Nominal Li filling levels by the end of the run campaign exceeded the porosity void fraction by 150%. Despite a nominal liquid level exceeding the capillary structure and peak current densities into the PFCs exceeding 100 kA m^{-2}, no macroscopic ejection events were observed. In addition, no substrate line emission was observed after achieving lithium-melt temperatures indicating the lithium wicks and provides a protective coating on the molybdenum porous layer. Impurity emission from the divertor suggests that the plasma is interacting with oxygen-contaminated lithium whether diverted on the LLD or not. A database of LLD discharges is analysed to consider whether there is a net effect on the discharges over the range of total deposited lithium in the machine. Examination of H-97L indicates that performance was constant throughout the run, consistent with the hypothesis that it is the quality of the surface layers of the lithium that impact performance. The accumulation of impurities suggests a fully flowing liquid lithium system to obtain a steady-state PFC on timescales relevant to NSTX.

(Some figures may appear in colour only in the online journal)

1. Introduction

Fusion reactors will eventually require a material from which to fabricate reactor components. To date, solid materials, most notably tungsten, has been the favoured material for reactor studies. Tungsten plasma-facing components (PFCs) are susceptible to several damage mechanisms in a reactor environment [1]. The most significant of these are transient melting and deformation and the second is net erosion and redeposition due to sputtering and plasma transport processes. An alternative to solid PFCs are those whose plasma-facing surface is composed of a liquid metal. Candidate liquid metals include lithium, tin and gallium as well as some mixtures of those metals such as Sn–Li [2]. These PFCs have the potential to alleviate the aforementioned damage mechanisms in solid PFCs and could lead to more robust fusion reactors.

There have, to date, been few examples of liquid metal PFCs in fusion plasma experiments. Lithium was first studied as a wall-conditioning material in TFTR but is largely considered to have been a conditioning technique applied to

solid, graphite PFCs [3]. T11-M reported experiments in 2000 on a *Capillary Porous System (CPS)* which presented liquid lithium to the plasma [4] and has continued those studies [5] and the CPS has also been used on the FTU [6]. CDX-U made use of a large-area limiter with a free surface of liquid lithium [7] and ISTTOK performed experiments on a free-surface jet of gallium [8]. None of these expreiments on liquid metal PFCs have been conducted in a diverted configuration (though KTM [9] is beginning such development).

Liquid metal PFCs include a set of technical challenges that require development before implementation into large machines. Lithium has been the favoured metal for these previously mentioned studies (except ISTTOK which uses gallium jets). The typical implementation previously has utilized a porous layer in contact with a reservoir of liquid lithium. The liquid metal wicks into the porous layer and maintains a liquid metal surface facing the incident plasma [10]. This type of limiter has been used on CDX-U, FTU and T11-M. Alternative approaches are to utilize a toroidal pool of liquid metal as was done in the CDX-U experiment after experiments with the porous-surface rail limiter [11]. While the pool was stable during discharges in CDX-U, a sample cup geometry was tested in the DIII-D tokamak showing instability [12]. In these tests an ELMy discharge resulted in macroscopic ejection of the lithium into the plasma exposing the substrate material (stainless steel or carbon). Plasma disruption followed after the ejection event. Stability of the liquid metal surface in the face of plasma heat and particle fluxes (both steady and transient) is of particular concern to the liquid metal approach.

The National Spherical Torus Experiment [13] (NSTX) has implemented a Liquid Lithium Divertor (LLD) module for experiments in the 2010 run campaign [14]. NSTX had previously utilized evaporated lithium onto graphite PFCs as a wall-conditioning technique and demonstrated performance improvements [15–17]. The maintenance of lithium efficacy throughout an extended pulse ($\tau_{pulse} > 1$ s) was a concern due to the known intercalation of lithium into graphitic materials [18]. A solid metal substrate was therefore considered to mitigate, if not eliminate, this process. In this paper we will describe the LLD as implemented in NSTX. The LLD did not exhibit macroscopic ejection of lithium from the surface and after liquefaction no substrate impurities were observed from the surface [19]. Discharges on the LLD exhibited evidence of gettered impurities, however, and make it difficult to consider these experiments a test of tokamak performance on a 'pure' liquid lithium PFC surface.

2. Apparatus and approach

A cross-section of the NSTX vessel is shown in figure 1. The LLD was installed in the lower vessel at large major radius (0.65–0.85 m in machine coordinates) where high-triangularity, high-performance discharges could be run on conventional graphite PFCs and experiments could be conducted on the LLD surface in a single run campaign. The LLD consists of four 22 cm wide plates each having a toroidal extent of 82.5°. The quadrants are separated toroidally by graphite tiles that contain diagnostics and other instrumentation. The LLD plates are made of 2.2 cm thick

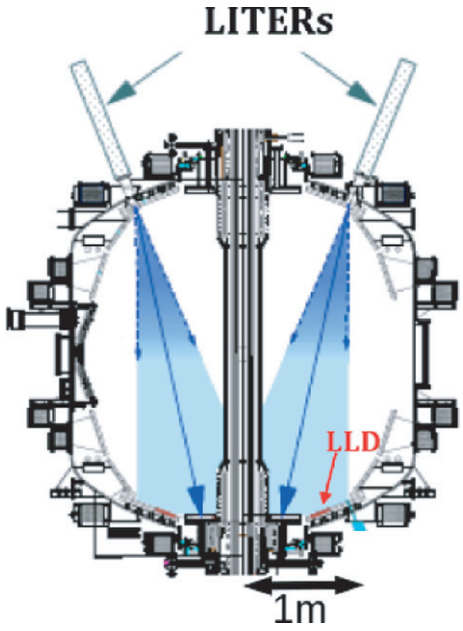

Figure 1. Cross-section of the NSTX vessel indicating location of the LLD installation in the lower vessel and LITER evaporation cones.

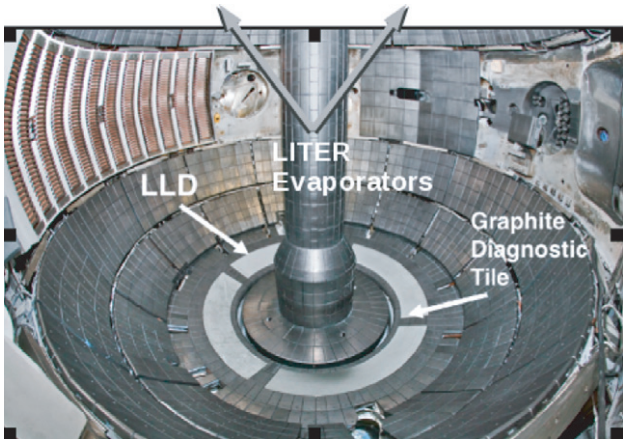

Figure 2. Image of the NSTX vessel interior. LLD plates are located in the lower-portion of the vessel. Three of four intersegment diagnostic breaks can also be seen. LITER evaporators are located at the vessel top as indicated in figure 1.

copper with a 0.25 mm stainless-steel liner bonded to the surface. This stainless steel provides a barrier between lithium applied to the surface of the LLD and the copper substrate which would otherwise be chemically corroded by the lithium [20]. A flame-sprayed, porous molybdenum layer of approximately 0.15 mm thickness forms the plasma-facing surface on top of the stainless-steel layer. An image of the interior of NSTX is shown in figure 2 indicating the LLD position as installed prior to the run campaign.

The LLD was intentionally installed to be slightly recessed of the adjacent graphite tiles. This was done to avoid any leading edges on the LLD itself which, by construction, only consisted of high-Z molybdenum on the front face whereas the side-walls consisted of a thin nickel plating over the stainless steel and copper bulk. The row of tiles inboard of the LLD are referred to as the 'bull-nose' tiles and extend from the LLD to

the Co-axial Helicity Injection (CHI) gap (62 cm). The LLD plate segments cover 330° of the divertor floor in total, or 92% of the circumference of the machine.

Porous molybdenum is used for several reasons. The first of which is to provide a low sputter-yield material to cover the stainless steel-layer on the LLD. Additionally, molybdenum is compatible with liquid lithium over a wide range of foreseeable temperatures in NSTX whereas previous studies have shown lithium can corrode stainless steel [21]. Finally, the porous molybdenum facilitates the wetting and subsequent spreading of liquid lithium over the LLD and also insures that surface tension forces are large relative to electromagnetic forces to retain the liquid lithium during plasma operations [22].

The lithium capacity of the porous LLD surface was estimated to be 37 g via image analysis of cross-sectional micrographs of the flame-sprayed material. The 2010 experiments were performed with the LLD filled with increasing amounts of deposited lithium, from a few per cent at the beginning of the run campaign to an estimated 160% of fill on the last day of the run (60 g). Each of the four LLD segments included embedded electrical heaters and thermocouples for monitoring heating. During operation, the thermocouples are disconnected immediately prior to a discharge and reconnected immediately following a discharge to avoid excessive currents to the heater control system. Due to this scheme, real-time thermocouple data is not available of the LLD segments; however, a change in temperature from before and after the discharge can be calculated. As previously mentioned, the LLD was filled with lithium via the LITER evaporator system. Estimates place the filling efficiency of the LLD at about 7% of the total evaporated lithium [23]. By the end of the run campaign, therefore, approximately 860 g of lithium had been deposited into the machine, 60 g of which was located on the LLD plates themselves. Typical operation in NSTX makes use of between 100 and 700 mg of lithium evaporated into the vessel over a 10 min interval for about 90% of the discharges in a run campaign.

A new set of Langmuir probes in the high-density Langmuir probe array (HDLP) were also implemented in the 2010 campaign and are located in one of the intersegment graphite diagnostic tiles. This probe array consists of 99 individual Langmuir probe tips arranged in a 3 × 33 pattern extending in radius from 62–72 cm in machine coordinates. Only a subset of the 99 probes are instrumented at any one time, but it is sufficient for the probes provide information on particle fluxes, plasma density and temperature of the plasma in their local vicinity. More information on the HDLP can be found in the literature [24–26]. The surface temperature of the LLD was monitored with the use of dual-band infrared thermography [27]. By using multiple infrared bands this system is capable of accounting for changes in emissivity of grey-body emitters and provide a more accurate surface temperature than a single-band system. Other diagnostics utilized include the typical suite of tools available on NSTX such as magnetic sensors (and associated EFIT reconstructions), divertor filter scopes and spectroscopy, and core measurements such as multi-point Thomson scattering and charge-exchange recombination spectroscopy.

During the 2010 NSTX experimental campaign, experiments dealing with the LLD itself were conducted over the course of the entire campaign at specific intervals. A typical plasma reconstruction is shown in figure 3. In these plasmas, a lower-single null discharge was formed with the outer strike point (OSP) near or impinging the LLD plates. When the OSP is not directly on the LLD, it is diverted onto the bull-nose tile immediately inboard of the LLD itself.

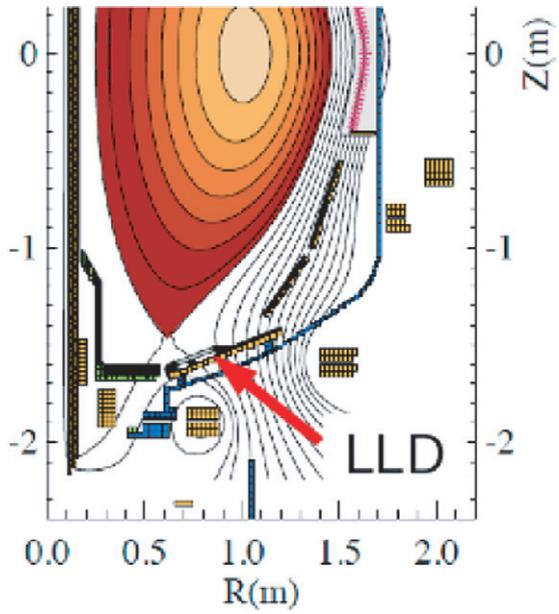

Figure 3. Typical equilibrium reconstruction for a discharge during LLD experiments. The outboard strike point was located in the vicinity of the LLD or directly impinging it as in this example.

A database of the available discharges has been assembled in the following manner. As multiple diagnostics are available with disparate time-base signals, a single, uniform time-base signal is constructed from the selected diagnostics. This is done by obtaining a time-base signal and dividing the signal into uniform segments of 200 ms in duration. The diagnostic signal is then averaged over the time window to provide a typical value for this time in the discharge. An example is shown in figure 4.

In some cases, spatial information is available in the underlying diagnostic, such as with multi-point Thomson scattering and Langmuir probes in the divertor target (as shown in the fourth panel of figure 4). In these instances, the data are arranged on flux surfaces and a composite time-base signal is generated. Flux surfaces are defined via the equilibrium reconstruction provided by EFIT [28]. We make use of the normalized poloidal flux coordinate, ψ_N, and assume toroidal symmetry as the divertor plasma is highly non-uniform as a function of the poloidal coordinate. Figure 4(*d*) shows such an example where multiple Langmuir probes fall within the range of $1.0 < \psi_N < 1.005$, but a single time-trace can be produced from all the data falling within this window. Details of this analysis procedure can be found in [26]. This region of ψ_N corresponds to immediately outboard of the separatrix in the outboard divertor. This allows one to compare signals on similar magnetic surfaces from shot-to-shot.

There is evidence that the plasma conditions in the divertor of NSTX are not toroidally symmetric due to variances in deposition thickness over the full-2π radians of the divertor floor as well as variances in the thermal response of the

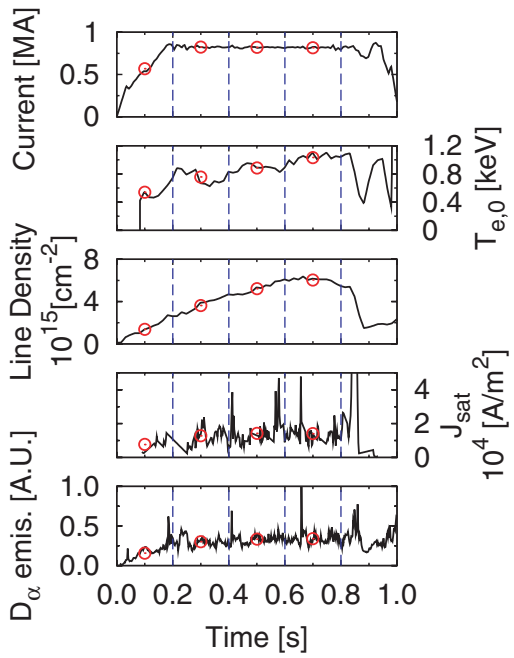

Figure 4. Example discharge (142521) showing full diagnostic signals (solid black line) and averaged values (red circles) within each time window (delineated by vertical lines). See text for details.

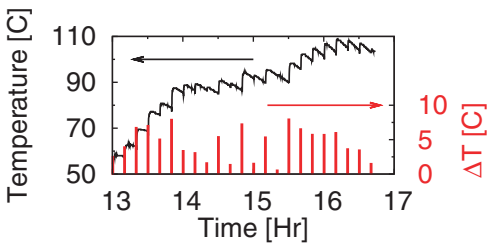

Figure 5. Example LLD temperature response during experiments. Mean temperature change for all four plates also shown. No active cooling was employed and resulted in a gradual rise in bulk temperature throughout the run day.

underlying substrate material [29]. These variances, however, do not impact the current study as the quantities examined are whole-machine integrated quantities (e.g. power crossing the last-closed flux surface (LCFS)) or from diagnostics with viewing angles that are large compared to the measured variances in toroidal symmetry (e.g. filterscope views of the lower divertor). In addition, the key variable considered here is whether the large-area LLD structure has a significant impact on plasma performance.

Figure 5 shows the temperature response of an LLD segment during a typical set of discharges. Each discharge deposits energy into the plate resulting in a temperature rise as indicated in the plot. The thermal insulation between the LLD segments is sufficient to use this temperature response for calorimetry. The energy rise of an LLD segment is given as:

$$\Delta E = m c_{\mathrm{p}} \Delta T, \tag{1}$$

where ΔE is the change in energy, m is the mass of the LLD plate, c_{p} is the specific heat of the copper and ΔT is the temperature rise from before the pulse to after. A mean heating power, $\overline{P_{\mathrm{LLD}}}$, delivered to the plate by the plasma during the discharge can also be calculated using the pulse duration, τ_{pulse}, as follows:

$$\overline{P_{\mathrm{LLD}}} = \frac{\Delta E}{\tau_{\mathrm{pulse}}}. \tag{2}$$

When calculating the H-factor, it is necessary to combine several variables for the calculation. In this work, we make use of the H-97L L-mode correlation [30] as it has been used to characterize confinement improvements in NSTX with the usage of lithium in the past [16]. The confinement scaling is defined as follows [30]:

$$\tau_E = 0.037 \times I_{\mathrm{P}}^{0.74} B_{\mathrm{T}}^{0.2} \kappa^{0.67} R^{1.69} A^{-0.31} n_{\mathrm{e}}^{0.24} M_{\mathrm{eff}}^{0.26} P^{-0.57}, \tag{3}$$

where τ_E is the energy confinement time, I_{P} is the plasma current, B_{T} is the toroidal field, κ is the plasma elongation, R is the major radius, A is the aspect ratio, n_{e} is the average density of the discharge, M_{eff} is the effective ion mass and P is the heating power corrected for any time-varying stored energy. Variables are set in units of (MA), (T), (m), (m^{-3}), (AMU) and (MW) for I_{P}, B_{T}, R, n_{e}, M_{eff} and P respectively. Shape factors are obtained with EFIT [28]. Density is obtained from Thomson scattering. The average ion mass is calculated with the NSTX CHERS diagnostic [31] in order to account for significant carbon impurity fractions in the NSTX discharges under ELM-free operation.

$$M_{\mathrm{eff}} = \frac{m_{\mathrm{D}} n_{\mathrm{D}} + m_{\mathrm{C}} n_{\mathrm{C}}}{n_{\mathrm{D}} + n_{\mathrm{C}}}, \tag{4}$$

where m and n are the ion mass and density, respectively, and subscripts $_{\mathrm{D}}$ and $_{\mathrm{C}}$ refer to deuterium and carbon, respectively.

In nearly all experiments conducted in the NSTX, fast-cameras are used to monitor the vessel interior as well as image the lower divertor. These fast-cameras can be filtered to specific spectral lines to obtain distributions of emission in the vessel in the 2D view of the camera.

3. Liquid metal stability

The feasibility of a free-surface, liquid metal PFC is dependent on the demonstration of a stable surface during operation. Several studies have been carried out in recent years on melt-layer motion. In the case of plasma-gun testing in QSPA, repeated plasma discharges resulted in significant melt-layer motion and splashing from the surface of a tungsten target [32]. Analysis of ejection indicates that the strong flows and plasma pressures present in QSPA give rise to Kelvin–Helmholtz instabilities that can eject droplets [33]. Plasma pressure can also result in motion of the free surface as indicated by experiments conducted on ASDEX-Upgrade [34]. Finally, currents injected into the PFC can also induce motion through the generation of $\vec{J} \times \vec{B}$ forces where the current can arise due to plasma scrape-off layer currents, disruption eddy-currents or thermionic emission due to high-temperature surfaces [35].

In addition to Kelvin–Helmholtz instabilities, a Raleigh–Taylor instability can also result in ejection of material from a surface [22]. As the derivation provided in [22] is abbreviated, we here make a more thorough presentation.

In the most general case, the Raleigh–Taylor instability arises when a body force directs a dense material into a less-dense material. In the case of a horizontal plate in a tokamak

divertor, currents flowing in the major radial direction will interaction with the toroidal field and produce a vertical force. Depending on the sign of the current and field, this force can act to destabilize the surface in the Raleigh–Taylor instability. A full derivation of such instabilities can be found in [36] and only minor modifications are required to include both magnetic field effects and surface tension stabilization of the liquid metal. Let us suppose we arrange two fluids with densities ρ_1 and ρ_2 on top of one another so that the interface lies in the xy-plane. Further, let us assume that gravity acts downwards and for the upper fluid to be the denser of the two: $\rho_2 > \rho_1$. For convenience, let us say that the magnetic field vector points in the x direction. One can begin with the general equations of motion for an incompressible fluid as follows [36]:

$$\nabla \cdot \vec{u} = 0 \tag{5}$$

$$\rho\left(\frac{\partial \vec{u}}{\partial t} + (\vec{u}\cdot\nabla)\vec{u}\right) = \rho\vec{X} - \nabla p + \vec{J}\times\vec{B} + \mu_f \nabla^2\vec{u}, \tag{6}$$

where $\vec{u}$ is the fluid velocity, $\rho\vec{X}$ is a body force due to an acceleration such as gravity, g, pressure is indicated by p, $\vec{J}\times\vec{B}$ is the force arising from currents, $\vec{J}$, interacting with an imposed field, $\vec{B}$, and the final term in equation (6) is the dissipation due to viscosity, μ_f. We split the Lorentz force into a component produced due to motion of the fluid through the magnetic material (here assumed to be of infinite conductivity) and those that can be generalized into a body force with acceleration, f. Expanding equations (5) and (6) into x, y and z components of velocity (u, v, and w respectively), one obtains:

$$\rho\frac{\partial u}{\partial t} = -\frac{\partial}{\partial x}\delta p \tag{7}$$

$$\rho\frac{\partial v}{\partial t} - \frac{\mu H}{4\pi}\left(\frac{\partial h_y}{\partial x} - \frac{\partial h_x}{\partial y}\right) = -\frac{\partial}{\partial y}\delta p \tag{8}$$

$$\rho\frac{\partial w}{\partial t} - \frac{\mu H}{4\pi}\left(\frac{\partial h_z}{\partial x} - \frac{\partial h_x}{\partial z}\right) = -\frac{\partial}{\partial z}\delta p - \delta\rho(g-f) \tag{9}$$

$$\frac{\partial \vec{h}}{\partial t} = H\frac{\partial \vec{u}}{\partial x} \tag{10}$$

$$\text{and}\qquad \frac{\partial}{\partial t}\delta\rho = -w\frac{\partial \rho}{\partial z}, \tag{11}$$

where perturbed fluid quantities from an assumed equilibium are denoted with δ and the perturbed magnetic field in direction i is denoted with h_i ($\mu\vec{H} = \vec{B}$ with magnetic permeability, μ). It can be shown that viscosity does not alter whether a given mode is Raleigh–Taylor unstable; it only affects the growth rate of the unstable modes [36]. We therefore eliminate the viscous term from the present analysis.

In the case of non-zero surface tension, Σ, acting at the fluid interface an additional term is added to the right hand side of equation (9) [36]:

$$\Sigma\left(\frac{\partial^2}{\partial x^2} + \frac{\partial^2}{\partial y^2}\right)\delta z_s \tag{12}$$

where z_s is the position of the interface. This term reflects the additional stress acting on the fluid due to the non-zero curvature and surface tension.

Normal modes are sought with the following form:

$$\exp(\mathrm{i}k_x x + \mathrm{i}k_y y + nt), \tag{13}$$

where $\mathrm{i} = \sqrt{-1}$, $k^2 = k_x^2 + k_y^2$ is the wavenumber of the disturbance with components in the x and y directions, and n is the growth rate (i.e. positive values of n indicate an unstable mode). After a series of algebraic reductions, the following equation governing the fluid is found:

$$D(\rho Dw) + \frac{\mu H^2 k_x^2}{4\pi n^2}(D^2 - k^2)w - k^2\rho w = -\frac{(g-f)k^2}{n^2}(D\rho)w + k^2\sum_s T_s w_s \delta(z - z_s), \tag{14}$$

where $D = \partial/\partial z$ is used for brevity. Integration over the boundary provides a jump condition:

$$\Delta_s(\phi) = \int_{s-}^{s+} D\phi\,\mathrm{d}z = \phi(z_s + 0) - \phi(z_s - 0), \tag{15}$$

where ϕ is some fluid quantity (e.g. density) that may be discontinuous across the boundary s. Evaluating equation (14) with this boundary condition one finds

$$\Delta_0(\rho Dw) + \frac{\mu H^2 k_x^2}{4\pi n^2}\Delta_0(Dw) = -\frac{k^2}{n^2}\left[(g-f)(\rho_2 - \rho_1) - k^2 T\right]w_0. \tag{16}$$

A solution for the differential equation $(D^2 - k^2)w = 0$ found in equation (14) that is convenient for use is given as:

$$w_1 = A\mathrm{e}^{+kz} \qquad \text{for } z < 0 \tag{17}$$

$$w_2 = A\mathrm{e}^{-kz} \qquad \text{for } z > 0 \tag{18}$$

which accommodates the needs that the velocity, w, vanish far from the fluid boundary and be continuous at the interface. Combining equations and applying the solution for w one obtains the result for the growth rate of an instability with wavenumber k:

$$n^2 = k(g-f)\left[\frac{\rho_2 - \rho_1}{\rho_2 + \rho_1} - \frac{k^2\Sigma}{(g-f)(\rho_2 + \rho_1)} - \frac{\mu H^2 k_x^2}{2\pi(g-f)(\rho_2 + \rho_1)k}\right]. \tag{19}$$

Equation (19) indicates several useful features. The first term indicates that the sum of accelerations g and f must result in an overall acceleration into the less-dense fluid, ρ_1, for an instability to occur. This is not sufficient, however, as the sum of terms in the square brackets $[\cdots]$ must also yield a net positive value (i.e. into the less-dense fluid) for the wave perturbation to be unstable. As we have begun the problem statement that $\rho_2 > \rho_1$, we can see the first term in the brackets is destabilizing due to the accelerations. The second term corresponds to the stabilizing force due to the surface tension of the fluid. (It is this term that causes small-diameter straws to retain a small amount of liquid after stirring a cup of coffee or tea.) Finally, the effect of the magnetic field is similar to that of surface tension in that it provides stability, *but only for field-aligned wave vectors*. When one appropriately orients a perturbation at the fluid interface, the effect of the magnetic field can be nullified, even in the case of a perfectly conducting fluid. The effect of this stabilization varies with the wavenumber (i.e. the wavelength) such that more stability is provided the larger (smaller) the wavenumber (wavelength) of the perturbation.

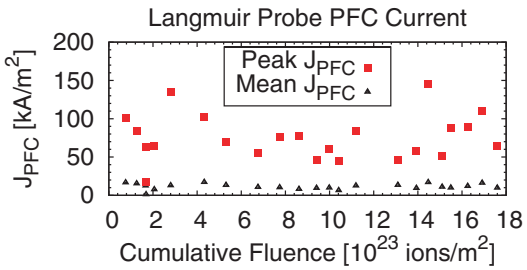

Figure 6. Quiescent and transient currents measured with the HDLP during a typical LLD run day. Each point represents an individual discharge where the mean current during the discharge is shown by the black triangles and the maximum value is shown by the red squares.

Equation (19) can be re-arranged after solving for the marginal stability condition ($n = 0$). The least stable modes will be those that are aligned orthogonal to the applied field and only stabilized by the surface tension. In the case of the LLD, we consider a $\vec{J} \times \vec{B}$ force acting upwards while gravity acts downwards. We further consider $\rho = \rho_2 \gg \rho_1$. One finds a critical wavenumber, k_{cr}, as follows:

$$k_{\mathrm{cr}} = \sqrt{\frac{jB - \rho g}{\Sigma}} \tag{20}$$

Alternatively, a critical current density can be obtained as a function of wave length ($k = 2\pi/\lambda$):

$$j_{\mathrm{cr}} = \frac{1}{B}\left(\frac{4\pi^2}{\lambda^2}\Sigma + \rho g\right). \tag{21}$$

In equation (21) one can see the effect of reduced wavelength of the perturbation.

4. Results and discussion

The first notable result from operation with the LLD is that no molybdenum influx was observed during most discharges. As reported in [19], early in the run, when evaporations had been performed on the LLD while cold, molybdenum emission from the divertor was observed during MHD events. After reaching temperatures above the lithium melting point (181 °C), no such molybdenum emission was again observed. This repeats the results reported with the CPS devices which also indicated protection of the substrate material with liquid lithium PFCs [10].

The next notable result is that *no macroscopic amounts of lithium were ejected from the LLD during the run campaign*. Figure 6 shows a set of measurements of the current entering grounded PFCs during a typical run day as obtained with the HDLP. A typical quiescent current in the SOL of NSTX is at a level of 10 kA m^{-2}. Transient currents due to disruptions and ELMs can create currents entering the PFC an order of magnitude above the quiescent level. In the worst-case scenario, 100% of these currents will close across flux surfaces through the PFC surface itself. This situation will result in the largest possible forces tending to destabilize the liquid.

Before the operating space of the LLD can be placed on a stability diagram, the expected wavelengths on the surface must be estimated. Scanning electron microscopy has been

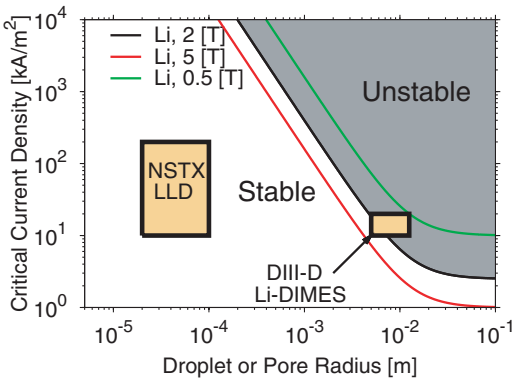

Figure 7. Stability diagram for a liquid metal under electromagnetic body forces (with gravity and surface tension stabilizing). NSTX LLD operating space indicated ($B_{\mathrm{T}} = 0.5$ T). Comparison with Li-DIMES experimental space also shown ($B_{\mathrm{T}} = 2$ T) [12]. No ejection events from the LLD were observed during the run campaign.

used on the porous, flame-sprayed molybdenum layer to generate an estimated pore size of ≈20 μm. An additional limit would be expected due to the depth of the fluid [22]. A conservative estimate on a droplet size limited by the fluid depth would place an upper-bound at about 100 μm. In the case of linear stability, then, the expected droplet sizes can be placed between $20 < r_{\mathrm{droplet}} < 100\,\mu$m.

Figure 7 shows the marginal stability curve as a function of droplet radius for a number of magnetic fields. Also shown in the figure is the approximate operating space of the NSTX LLD as defined by the typical PFC currents measured during discharges and the estimated range of possible droplet radii. As can be seen, the NSTX LLD is predicted to be completely stable against Raleigh–Taylor instabilities that might tend to eject droplets into the plasma. This is consistent with the lack of any observed ejection events. In the same figure, we make a comparison with results from the DIII-D Li-DIMES experiment which exhibited ejection of the lithium from a 25 mm diameter, 1 mm thick lithium sample at much lower injected current densities [12]. From the stability diagram, one can see that the Li-DIMES experiment is only marginally stable. The strategy of reducing pore size to stabilize a liquid metal was also implemented with the liquid lithium Capillary Porous System developed by Red Star [10]. In experiments in T11-M, it was found that by reducing the pore size of the mesh used in the CPS, droplet ejection could be eliminated. *This usage of a porous substrate for stabilization of the free-surface liquid metal has now been demonstrated in a diverted tokamak.*

The amount of power absorbed onto the LLD depends on the strike-point position. Figure 8 shows a comparison of absorbed power, as determined by calorimetry, as a function of strike-point position. In figure 8(*a*) the total absorbed power is shown and in figure 8(*b*), the fraction of power absorbed by the LLD of that crossing the LCFS is shown. For this shape of discharge and divertor flux expansion, probe analysis has indicated that the particle flux footprint is approximately 4–6 cm. With this wide particle flux, a transition region between fully diverted onto the LLD and fully off the LLD could be expected between 65 and 70 cm and this is indicated in the data. For these discharges, then,

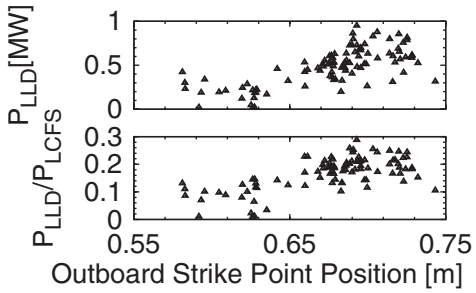

Figure 8. Mean heating power deposited in the lower divertor at the LLD location as determined by thermocouple calorimetry. Below, the same data as in (*a*) except as a fraction of the power crossing the LCFS. LLD nominal inner edge is at 0.65 cm.

we can show that MW level heating powers were impinging the LLD and that approximately 25% of the power exiting the LCFS resulted in heating of the LLD when diverted onto it. IR thermography also indicates significant heat fluxes in the range of 2–10 MW m^{-2} were typical of these discharges which is consistent with the estimated power density for a 4–6 cm heating region. Post-mortem analysis of the LLD plates indicated that no failure of the copper–stainless steel–porous molybdenum structure had occurred despite the large heat fluxes (and associated thermal stresses) and electromagnetic forces acting on the plates. The LLD therefore demonstrates a liquid metal PFC at reactor-relevant heat-flux levels in the diverted configuration. This is consistent with laboratory experiments that also demonstrated protection of the substrate by lithium coatings and survival of multisecond exposures to 1.5 MW m^{-2} heat fluxes [37].

When comparing $\overline{P_{\mathrm{LLD}}}$ to the power crossing the LCFS, P_{LCFS}, one would generally include significant loss terms that might occur from the LLD. Surface temperatures on the LLD typically peak from 300–400 °C even by 700 ms into the discharge [38] with temperatures peaked at the strike point. As the LLD design is thermally insulated, this eliminates conduction on the time scale of the plasma discharge. One can calculate radiative losses, P_{rad}, from the top surface of the LLD as follows:

$$P_{\mathrm{rad}} = \sigma \epsilon A_{\mathrm{surf}} (T_{\mathrm{surf}}^4 - T_{\mathrm{amb}}^4) \tag{22}$$

where σ is the Stefan–Boltzmann constant (5.67×10^{-8} W m^{-2} K^{-4}), ϵ is the surface emissivity, A_{surf} is the emitting surface area, T_{surf} and T_{amb} are the surface and ambient temperatures respectively. As a worst-case estimate, we take the entire front face of the LLD to be 400 °C and the surface emissivity to be unity with ambient temperature of 20 °C. This yields $P_{\mathrm{rad}} \approx 0.01$ MW which is insignificant compared to the mean heating powers measured (see figure 8). Similarly, evaporative power losses, P_{evap} can be estimated using the Langmuir formula for evaporation and known lithium vapour-pressures [39] such that

$$P_{\mathrm{evap}} = h_{fg} \frac{p_v}{\sqrt{2\pi m_{\mathrm{Li}} k T_{\mathrm{surf}}}} \cdot \frac{M_{\mathrm{Li}}}{A_{\mathrm{v}}} \tag{23}$$

where h_{fg} is the heat of vaporization, m_{Li} is the mass per lithium atom, k is the Boltzmann constant, M_{Li} is the molar mass of lithium and A_{v} is Avogadro's number. The

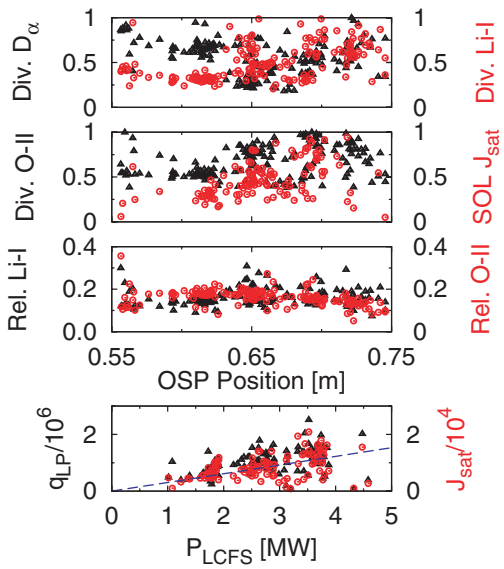

Figure 9. Divertor filterscope signals as a function of strike-point radius (0.4–0.6 s). (*a*) and (*b*) show the relative emission for D-alpha, Li I, and O II lines as well as the Langmuir probe J_{sat} for the region $1.0 < \psi_{\mathrm{N}} < 1.005$. Data in (*a*) and (*b*) are normalized to 1 to emphasize any qualitative structure in the data. Flux (heat or particle) are shown to be roughly proportional to the exhaust power in the machine in (*d*). Linear least-squares fit of $f(x) = ax$ is shown. Relative emission of Li I or O II normalized to exhaust power versus strike-point position in (*d*).

vapor pressure is given by $\ln(p_{\mathrm{v}}) = 26.89 - 18880/T_{\mathrm{surf}} - 0.4942 \ln(T_{\mathrm{surf}})$ in Pa. Again applying a worst-case estimate that the entire front face is at an elevated temperature of 500 °C, one finds the evaporated power to be $P_{\mathrm{evap}} \approx 0.003$ MW which is negligibly small compared to the incident heating power. At the observed temperatures, therefore, we conclude that the mean heating power derived from this method is not significantly affected by radiative or evaporative power losses.

Plasma diagnostics indicated that only subtle changes were occurring despite the change from carbon to molybdenum substrate. An examination of the divertor emission of several spectroscopic lines is shown in figure 9 as a function of the strike-point location. In transitioning to the LLD, a slight increase in the lithium and oxygen signals is observed as well as an increase in the probe J_{sat} in the near SOL. The probe fluxes are expected to be roughly proportional to the power crossing the LCFS if the electron temperature of the divertor is not changing to a large degree. This is, indeed, the case using the classical interpretation of the Langmuir probe signals [26] and both a Langmuir probe power flux or J_{sat} are roughly proportional to P_{LCFS}. One can the normalize the divertor emission signals to remove bias due to increased P_{LCFS} or J_{sat} and replot the data in figures 9(*a*) and (*b*) and this is shown in figure 9(*c*). One can see in the data that very little difference is now present in those discharges diverted over the LLD or onto the graphite bull-nose tiles.

Oxygen is a prevalent contaminant in lithium experiments. In the PISCES-B linear plasma device, extensive plasma cleaning was required to remove the oxygen [40]. In addition, laboratory tests have shown that in the presence of 1×10^{-6} Torr

partial pressures of water vapour, oxygen-containing surface layers will form in about 10 s [41]. Intershot pressure in the NSTX vacuum vessel is of order 1×10^{-7} Torr and the intershot time is about 600 s, providing ample time for surface oxygen layers to form. The slow filling process by evaporation in NSTX is therefore prone to contamination by background gases and reduces the likelihood that any LLD discharges could be considered a fair test of a 'pure' liquid lithium PFC.

It is reasonable to consider the effect surface contamination has upon the estimates of the free-surface stability presented in section 3. It is a common effect in liquid metals that impurities can have a surfactant action and tend to reduce the value of surface tension [42, 43]. This fact is often exploited in welding as a means of controlling melt-pool motion [44]. In the case of liquid lithium, segregation of oxygen has been observed which indicates a reduced value of surface tension when this impurity is present [45]. From equation (21) one can see that the critical current density is proportional to the value of surface tension. Reduction of the surface tension from that of pure lithium would tend to move the marginal stability curves to the left of figure 7. A worst-case estimate for surface tension is suggested by Bastasz and Whaley as the surface tension of pure oxygen, $\Sigma_O \approx 0.02\,\mathrm{N\,m^{-1}} \approx \Sigma_{Li}/16$. Utilizing this value in equation (21) would firmly place the DIII-D case into the unstable region, however the NSTX LLD operational space remains in the stable region by about a factor of 10 in current density.

Further indication of this surface contamination is seen in the behaviour of confinement time over the entire set of LLD discharges for the year. We show in figure 10 a summary of the database for a set of selected entries. Experiments were largely conducted in three groups at the beginning, middle and end of the campaign with a large variance in the amount of total lithium in the machine. A cursory look at a calculated confinement time from equilibrium reconstructions might lead one to consider performance to have decreased. However, normalizing against ITER97 L-mode scaling [30] indicates that performance at the beginning of the run was nearly identical with that at the end of the run campaign. If the relevant quality of the lithium in the machine is determined by the contamination rate of the lithium surface, which is much shorter than the inter-discharge timescale, then one would expect large quantities of evaporated lithium not to significantly alter the machine performance and this is consistent with the data from the FY2010 run campaign.

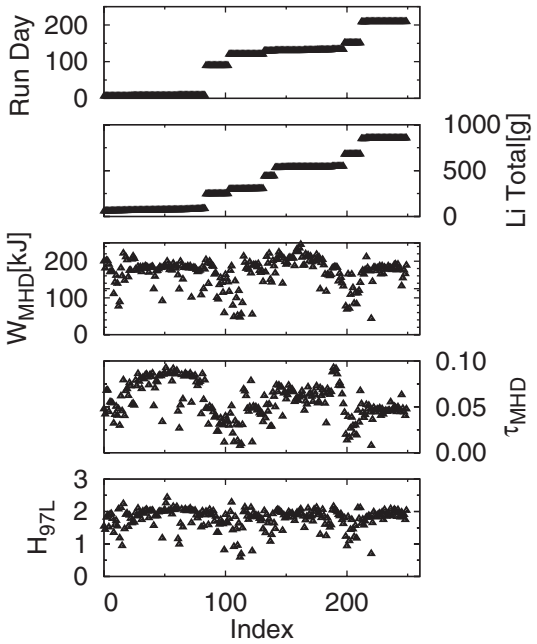

Figure 10. Selected entries from the LLD experimental database. Run day is the number of days since the beginning of the experimental campaign, Li Total is the integrated amount of lithium evaporated into the vessel, W_{MHD} is the plasma stored energy, τ_{MHD} is the energy confinement time, H-97L is the H-factor compared to the ITER 97L global confinement scaling [30]. W_{MHD}, τ_{MHD} and H-97L taken as the average between 400–600 ms.

5. Conclusions and future work

The NSTX LLD campaign has resulted in several important results related to the implementation of liquid metal PFCs. First, the LLD confirmed the result on limiter machines that liquid lithium provides a protective layer over a high-Z metal substrate. Next, the LLD demonstrated a stable liquid metal using a porous substrate for the first time in a diverted tokamak. In addition to the liquid metal stability, the overall construction of a porous metal substrate was able to successfully operate the entire run year without evidence of damage during post-mortem analysis. Finally, there are indications that the plasma response over the LLD is not distinguishable from plasmas diverted over the graphite tiles immediately adjacent. This is consistent with a nearly constant H-factor throughout the run campaign. Further, laboratory studies indicate that oxygen-containing impurity layers form on comparable (if not shorter) timescales as a typical NSTX shot sequence [41]. The hypothesis that it is the quality of the lithium surface that impacts plasma performance is consistent with the observed independence of confinement versus the total quantity of lithium in the machine.

The need to mitigate the accumulation of impurities on the surface of the lithium PFCs is strongly suggested by this data set. A fully flowing liquid lithium divertor would provide a means of removing impurities continuously from the surface and bulk of the lithium in the vessel. In addition, bulk cleaning of lithium has been demonstrated on PISCES-B [40] and may be possible with longer pulse-lengths in the NSTX-U. Development is underway for a fully flowing system in the long-range planning of NSTX-U while near-term experiments examining local transport of lithium and its impurities is underway in the laboratory and on linear test-stands.

Acknowledgments

M.A.J. would like to thank R. Axford (U-Illinois) for useful discussions on the Raleigh–Taylor analysis presented in this work. This work supported by USDOE contracts DE-AC02-09CH11466, DE-AC05-00OR22725, DE-AC52-07NA27344, DE-FG02-99ER54524, DE-FG02-08ER54990 and DE-AC04-94AL85000.

References

[1] Lipschultz B. *et al* 2012 *Nucl. Fusion* **52** 123002
[2] Abdou M.A. *et al* 2001 On the exploration of innovative concepts for fusion chamber technology *Fusion Eng. Des.* **54** 181–247
[3] Snipes J.A. *et al* 1992 Wall conditioning with impurity pellet injection on TFTR *J. Nucl. Mater.* **196–198** 686–91
[4] Evtikhin V.A., Lyublinski I.E., Vertkov A.V., Yezhov N.I., Khripunov B.I., Sotnikov S.M., Mirnov S.V. and Petrov V.B. 2000 Energy removal and MHD performance of lithium capillary-pore system for divertor target application *Fusion Eng. Des.* **49–50** 195–9
[5] Mirnov S.V. *et al* 2011 *J. Nucl. Mater.* **415** S417–20
[6] Apicella M.L., Mazzitelli G., Pericoli Ridolfini V., Lazarev V., Alekseyev A., Vertkov A., Zagórski R. and the FTU Team 2007 First experiments with lithium limiter on FTU *J. Nucl. Mater.* **363–365** 1346–51
[7] Majeski R. *et al* 2003 CDX-U operation with a large area liquid lithium limiter *J. Nucl. Mater.* **313–316** 625–9
[8] Gomes R.B. *et al* 2011 *J. Nucl. Mater.* **415** S989–92
[9] Tazhibayeva I., Pivovarov O., Shapovalov G. and Azizov A. 2008 Tokamak KTM progress activity for preparation on first plasma start-up Geneva, 2008 *22nd IAEA Fusion Energy Conf. (Geneva, Switzerland, 2008)* FTP/P6-08 www-naweb.iaea.org/napc/physics/FEC/FEC2008/html/index.htm
[10] Evtikhin V.A. *et al* 2002 Lithium divertor concept and results of supporting experiments *Plasma Phys. Control. Fusion* **44** 955–77
[11] Kaita R. *et al* 2007 Low recycling and high power density handling physics in the current drive experiment-upgrade with lithium plasma-facing components *Phys. Plasmas* **14** 056111
[12] Whyte D.G., Evans T.E., C. Wong P.C., West W.P., Bastasz R., Allain J.P. and Brooks J.N. 2004 Experimental observations of lithium as a plasma-facing surface in the DIII-D tokamak divertor *Fusion Eng. Des.* **72** 133–47
[13] Ono M. *et al* and the NSTX Team 2000 Exploration of spherical torus physics in the NSTX device *Nucl. Fusion* **40** 557–61
[14] Kugel H.W. *et al* 2012 *Fusion Eng. Des.* **87** 1724–31
[15] Bell M.G. *et al* 2009 *Plasma Phys. Control. Fusion* **51** 124054
[16] Maingi R. *et al* 2012 *Nucl. Fusion* **52** 083001
[17] Kaye S.M., Gerhardt S., Guttenfelder W., Maingi R., Bell R.E., Diallo A., LeBlanc B.P. and Podesta M. 2013 The dependence of H-mode energy confinement and transport on collisionality in NSTX *Nucl. Fusion* **53** 063005
[18] Itou N. *et al* 2001 *J. Nucl. Mater.* **290–293** 281–5
[19] Soukhanovskii V.A. *et al* 2010 *Rev. Sci. Instrum.* **81** 10D723
[20] Lyon R.N. (ed) 1950 *Liquid-Metals Handbook* 2nd edn (Washington, DC: United States Office of Naval Research) US Government Printing Office
[21] Katsuta H. *et al* 1977 *J. Nucl. Mater.* **71** 95–104
[22] Jaworski M.A. *et al* 2011 *J. Nucl. Mater.* **415** S985–8
[23] Kugel H.W. *et al* 2010 *Fusion Eng. Des.* **85** 865–73
[24] Kallman J., Jaworski M.A., Kaita R., Kugel H. and Gray T.K. 2010 High density Langmuir probe array for NSTX SOL measurements under lithiated divertor conditions *Rev. Sci. Instrum.* **81** 10E117
[25] Jaworski M.A., Kallman J., Kaita R., Kugel H.W., LeBlanc B., Marsala R. and Ruzic D.N. 2010 Biasing, acquisition and interpretation of a dense Langmuir probe array in NSTX *Rev. Sci. Instrum.* **81** 10E130
[26] Jaworski M.A. *et al* 2012 Modification of the electron energy distribution function during lithium experiments on the national spherical torus experiment *Fusion Eng. Des.* **87** 1711–8
[27] McLean A.G. *et al* 2012 *Rev. Sci. Instrum.* **83** 053706
[28] Sabbagh S.A. *et al* and the NSTX Research Team 2001 Equilibrium properties of spherical torus plasmas in NSTX *Nucl. Fusion* **41** 1601–11
[29] Scotti F., Roquemore A.L. and Soukhanovskii V.A. 2012 Full toroidal imaging of non-axisymmetric plasma material interaction in the National Spherical Torus Experiment divertor *Rev. Sci. Instrum.* **83** 10E532
[30] Kaye S.M. *et al* 1997 *Nucl. Fusion* **37** 1303–28
[31] Podestà M. *et al* 2012 *Nucl. Fusion* **52** 033008
[32] Federici G. *et al* 2005 *J. Nucl. Mater.* **337–339** 684–90
[33] Bazylev B. *et al* 2009 *Phys. Scr.* **T138** 014061
[34] Krieger K. *et al* 2011 *Phys. Scr.* **T145** 014067
[35] Coenen J.W. *et al* 2011 *Nucl. Fusion* **51** 083008
[36] Chandrasekhar S. 1961 *Hydrodynamic and Hydromagnetic Stability* (New York: Dover)
[37] Abrams T., Jaworski M.A., Kallman J., Kaita R., Foley E.L., Gray T.K., Kugel H., Levinton F., McLean A.G. and Skinner C.H. 2013 Response of NSTX liquid lithium divertor to high heat loads *J. Nucl. Mater.* **438** S313–6
[38] McLean A.G. *et al* 2013 Measurement and modeling of surface temperature dynamics of the NSTX liquid lithium divertor *J. Nucl. Mater.* **438** S397–400
[39] Abdou M.A. *et al* 1999 On the exploration of innovative concepts for fusion chamber technology: APEX interim report *Technical Report UCLA-ENG-99-206* University of California, Los Angeles
[40] Doerner R. *et al* 2001 *J. Nucl. Mater.* **290–293** 166–72
[41] Skinner C.H., Sullenberger R., Koel B.E., Jaworski M.A. and Kugel H.W. 2013 Plasma facing surface composition during NSTX Li experiments *J. Nucl. Mater.* **438** S647–50
[42] Adamson A. and Gast A. 1997 *Physical Chemistry of Surfaces* (New York: Wiley)
[43] Nornberg M.D., Ji H., Peterson J.L. and Rhoads J.R. 2008 A liquid metal flume for free surface magnetohydrodynamic experiments *Rev. Sci. Instrum.* **79** 094501
[44] Do-Quang M., Amberg G. and Pettersson C.-O. 2008 Modeling of the adsorption kinetics and the convection of surfactants in a weld pool *J. Heat Transfer* **130** 092102
[45] Bastasz R. and Whaley J.A. 2004 Surface composition of liquid metals and alloys *Fusion Eng. Des.* **72** 111–9